Xu *et al. Chin. J. Mech. Eng.* (2019) 32:29
https://doi.org/10.1186/s10033-019-0346-6

Chinese Journal of Mechanical Engineering

ORIGINAL ARTICLE Open Access

Investigation on LCF Behavior of Welded Joint at Different Temperatures for Bainite Steel

Ke Xu, Xiongfei Wang, Haichao Cui and Fenggui Lu*

Abstract

The current research of low cycle fatigue (LCF) is mainly focused on the components with uniform microstructure. Compared with these typical components, LCF behavior of welded components are more complex due to their great gradient microstructure, especially for different temperature. In this paper, LCF properties were conducted on the welded joint at different temperatures for bainite steel, and the failure mechanism was systematically discussed. Fatigue parameters derived from fitting curves indicated that welded joint had worse plastic deformation resistance and experienced more significantly strain hardening effect at 300 °C. The joint failed in the weld metal at room temperature, which attributed to the softening in weld metal combined with cyclic strain hardening effect in heat-affected zone, which meant the joint was more sensitive with the hardness at this condition. When it came to 300 °C, more cracks appeared near to HAZ and the heterogeneous distributed surface inclusion was responsible for the fracture transition to HAZ adjacent to bainite steel rather than the softest zone in HAZ, reflecting the joint was more sensitive with the surface inclusion at 300 °C. This research could support the design on loading of welded component at different temperature, and further ensure the safe operation.

Keywords: Low cycle fatigue, Welded joint, Different temperatures, Failure mechanism

1 Introduction

In the past few years, nuclear power plant has underwent a rapid development as its extraordinary high efficiency, reliable security as well as so-called environmental friendly facilities [1, 2]. As the most critical component of the turbines, the long term reliability of the rotor must be ensured due to the ultra-severe working conditions, including the long time thermal exposure, the complex cyclic loading and even the probable neutron damage [3–6]. Generally, the stress imposed on the structural components induced by the cyclic loading will undoubtedly exceed the yield strength, which will emerge irreversible plastic deformation on the material thus belong to the research field of low cycle fatigue (LCF) behavior [7–10].

Actually, a considerable number of structural components' failure can be attributed to the LCF damage, especially for the steam rotors during start/stop stage and power transient period [11–17]. A series of parameters, including the temperature [18], the strain rate [19], the strain amplitude [20], etc., could influence the LCF behavior of the material. Mishnev et al. [21] investigated the microstructure evolution of 10% Cr steel at different temperatures (20–650 °C) under LCF conditions. The results indicated that the 10% Cr steel was susceptible to cyclic softening at a wide temperature range. The fatigue failure could be contributed to the coarsening of laths and the decrease of dislocation density at 20 to 550 °C, while the transformation of the tempered martensite lath to sub-grains at 550 and 650 °C was responsible for the softening behavior and the finally fatigue failure. LCF tests of 9Cr-1Mo steel with different strain rates (10^{-3}/s and 10^{-2}/s) under LCF loading were performed by some researchers [22–24] at three temperatures (RT, 300 °C and 600 °C), finding that the fatigue life and the plastic strain amplitude increased at higher strain rates for each temperature, which can be attributed to higher fatigue crack growth rate induced by the dynamic strain aging (DSA). In our previous study [25] on the LCF behavior of martensite-bainite dissimilar welded joint at 500 °C, the

*Correspondence: Lfg119@sjtu.edu.cn
Shanghai Key Laboratory of Materials Laser Processing and Modification, School of Materials Science and Engineering, Shanghai Jiao Tong University, Shanghai 200240, China

fatigue failure shifted from bainite BM to OTZ with the increasing strain amplitude, reflecting the load distribution on each zone varied greatly for the inhomogeneous structure with different strain amplitudes.

Till now, numerous studies have been conducted on LCF behaviors on the base materials, which becomes more challenge when it comes to the welded joints with inhomogeneous microstructure and heterogeneous distributed defects as well as the severe working conditions [26–29]. As a kind of low-alloy high toughness bainite steel, NiCrMoV steel is widely used to manufacture the welded component since its excellent mechanical properties and competitive costings [30]. Investigations about the NiCrMoV welded joint have been conducted about the frequency effect on high cycle fatigue behavior and very high fatigue properties at moderate temperature [31], the fatigue crack growth behavior [32, 33], the effect of long-term aging on microstructure evolution in heat affected zone [34] and toughness [35]. Obviously, only few studies about the LCF behavior of NiCrMoV welded joint have been reported let along ambiguous failure mechanism at different temperatures.

In the present work, the candidate material is a kind of low-alloy high toughness bainite steel with big thickness, which was manufactured by narrow gap arc welding technology. The temperature-dependent LCF test was carried out and its behavior will be analyzed by microstructure characterization, data fitting, fracture morphology observation and comparison of micro-hardness distribution. Finally, we attempt to clarify the mechanism of failure location transition at different temperatures.

2 Experimental Procedure

2.1 Experimental Materials

In this work, low-alloy high toughness bainite steel with the thickness of 100 mm employed as base metal (BM) to manufacture welded joint. The chemical composition of the BM and the weld metal listed in Table 1. The weld joint was fabricated by the narrow gap arc welding technology accompanied with the multi-layer and multi-pass techniques, which was followed by post-weld heat treatment (PWHT) that aims to release the residual stress and homogenize the microstructure of the welded joint.

2.2 LCF Test

The geometry of the specimen for low cycle fatigue test is shown in Figure 1. Before the LCF test, the gauge area of the specimen was polished smoothly to eliminate the surface defects. Pull-push (axial) strain-controlled fatigue tests following the standard ISO 12016:2003 were then performed on the MTS NEW 810 fatigue testing system at room temperature and 300 °C. The triangular waveform was selected with the strain ratio of $R=-1$, the constant strain rate of 2×10^{-3} and the sampling interval of 0.05 s. The temperature fluctuation during the test was maintained within ±2 °C. Fatigue tests were conducted duplicately for each strain amplitude to improve the accuracy of data. Fatigue life (Nf) is defined as the number of cycles when the specimen fractures or the maximum stress decreases by 50%. After the LCF test at different temperatures, the failure locations will be evaluated before the subsequent analysis.

2.3 Microstructure Characterization

Before the LCF test, Microstructure characterization was conducted on optic microscope (OM, Zeiss Imager A2m) after being etched by A (a solution of 4% HNO3+CH3CH2OH). Micro-hardness distribution across the joint was tested by a hardness tester (Zwick/Roell) with a constant load of 9.8 N and holding time for 15 s. After the LCF test, micro-hardness from the BM to the middle of WM was compared to clarify the load

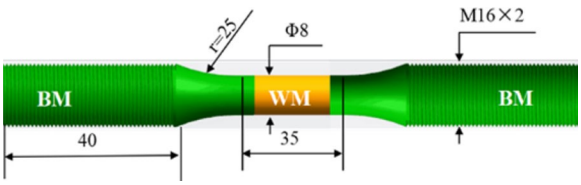

Figure 1 Geometry of the specimen for low cycle fatigue test (Unit: mm)

Table 1 Chemical composition of the base metals and the weld metal (wt%)

Materials	C	Si	Mn	P	S
BM	≤0.30	0.14	0.19	0.0041	≤0.15
WM	<0.12	0.40	1.41	0.0075	<0.01
Materials	**Cr**	**Mo**	**V**	**Ni**	**Cu**
BM	2.21	0.68	0.0634	2.11	≤0.17
WM	0.59	0.47	0.0028	2.10	<0.1

distribution for each zone at various conditions as well as determining the precise failure location. The fracture surface of the failed specimens was examined by SEM (JSM 7600F). Energy dispersive X-ray spectroscopy (EDS, INCA) was also carried out to detect the chemical composition of the crack initiation as well as trying to depict the failure transition mechanism at different temperatures.

3 Results and Discussion

3.1 Cyclic Stress-Strain Behavior and Fatigue Life

The cyclic stress-strain behavior could be described by the following equation originated from Ramberg-Osgood equation:

$$\frac{\Delta\varepsilon}{2} = \frac{\Delta\sigma}{2E} + \left(\frac{\Delta\sigma}{2K'}\right)^{\frac{1}{n'}}, \tag{1}$$

where $\Delta\sigma/2$ is the middle-life stress amplitude, $\Delta\varepsilon/2$ is the total strain amplitude, K' is the cyclic strength coefficient and n' is the cyclic hardening exponent. Figure 2 shows the relationship of stress amplitude and total strain amplitude, as can be seen, the data points fit better with the acquired curves at different temperatures. The K' and n' derived from two temperatures are listed in Table 2. It could be seen that the cyclic strength coefficient and the cyclic hardening exponent are much bigger compared to that of room temperature, it means the welded joint experiences more significantly strain hardening effect, which could be attributed to the formation of precipitates or carbides and its interactions with dislocations even though the temperature softening effect at elevated temperature.

The total strain amplitude consists of elastic and plastic strain amplitude in LCF analysis. Dependent equations were proposed between elastic/plastic strain amplitude and fatigue life by different researchers. Figure 3 represent the relationship between the strain amplitude and the number of reversals to failure at two temperatures by the Manson-Coffin equation, which is mathematically defined as Eq. (2):

$$\frac{\Delta\varepsilon}{2} = \frac{\Delta\varepsilon_e}{2} + \frac{\Delta\varepsilon_p}{2} = \frac{\sigma_f'}{E}(2N_f)^b + \varepsilon_f'(2N_f)^c, \tag{2}$$

where σ_f' is the fatigue strength coefficient, E is the Young's modulus, b is the fatigue strength exponent, ε_f' is the fatigue ductility coefficient, c is the fatigue ductility exponent and N_f is the number of cycles to failure.

The fatigue parameters at two temperatures are listed in Table 2. We can Figure out that the fatigue strength coefficient and the fatigue strength exponent at two temperatures are very close, reflecting the welded joint has

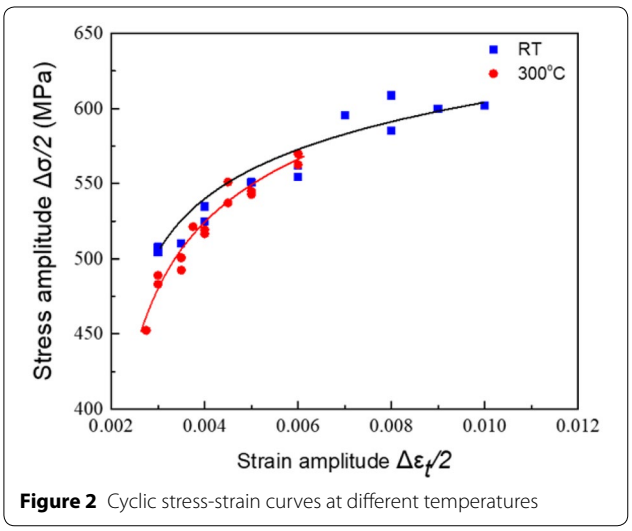

Figure 2 Cyclic stress-strain curves at different temperatures

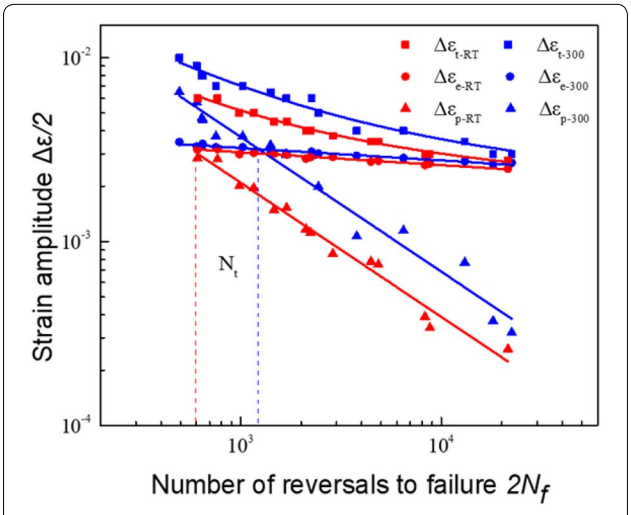

Figure 3 Strain amplitude-life curves at two different temperatures

Table 2 Low cycle fatigue parameters at two different temperatures

	σ_f' (MPa)	b	ε_f'	c	n'	K'
RT	998.4	− 0.068	0.3617	− 0.660	0.0666	842.0
300 °C	925	− 0.070	0.3251	− 0.731	0.0833	920.4

similar elastic strain behavior. While the joint has larger fatigue ductility coefficient and fatigue ductility exponent at room temperature, which indicates the joint has better plastic deformation resistance than that of elevated temperature. Finally, the intersection point corresponding to transition life of 1290 cycles (Nt) exists in RT but only 610 cycles in 300 °C as the fatigue life is very short at strain amplitude of 0.6% at 300 °C.

3.2 Cyclic Deformation Behavior

Generally, the cyclic deformation behavior represents the stress alteration of the material under cyclic loading conditions and it can include hardening stage, saturation stage and softening stage. The proportion of each stage depends on the original microstructure as well as the microstructure evolution during the cycling conditions.

Figure 4(a) and (b) show the stress amplitude variation tendency at various strain amplitudes at two temperatures, respectively. At room temperature, the data are obtained in the range of strain amplitude from 0.3% to 1.0%. While at 300 °C, the data are obtained in the range of strain amplitude from 0.275% to 0.6%. As can be seen, the stress amplitude increases with the increasing strain amplitude while the fatigue life decreases. At RT in Figure 4(a), the joint displays a stable period for the majority of life followed by a sudden softening behavior for the remaining life at strain amplitude of 0.3%, while it exhibits a continuous and gradual softening behavior followed by a sudden softening behavior at strain amplitude above 0.3%. When it turns to elevated temperature in Figure 4(b), the joint displays a stable period for almost 90%N_f followed by a sudden softening behavior at strain amplitude of 0.275% which only covers about 10%N_f. For strain amplitude from 0.3% to 0.5%, a continuous and gradual softening behavior followed by a sudden softening behavior is observed. While at strain amplitude of 0.6%, the joint shows a stable period in the first few cycles the followed by a slightly hardening effect and ends up with a continuous and gradual softening behavior.

3.3 Microstructure Characterization

Microstructure characterization of the welded joint is depicted in Figure 5. Figure 5(c) displays the overall microstructure across the welded joint, which can be divided into BMs, WM and HAZs. The width of the WM is about 20 mm and a typical multi-layer and double-pass feature can be observed. As shown in Figure 5(a) and (b), tempered granular bainite as the main microstructure of BM and WM with different grain size, and few blocky ferrite could be found in WM. As illustrated in Figure 5(d) and (e), HAZ can be further divided into coarse grain zone (CGZ) and fine grain zone (FGZ). The microstructure of the CGZ and FGZ are both tempered martensite. The austenite grains were larger in the CGZ due to the heating peak temperature was even higher than that of the FGZ. The BM was suffered from the heat treatment of quenching and high-temperature tempering, the over-tempering zone (OTZ) will occur under welding thermal cycle, which could be determined by hardness test due to no obvious microstructure difference with BM .

3.4 Failure Location and Micro-hardness Test

After the LCF test, all the specimens fails in the middle of the WM at RT, while the failure locations transferred to BM side at 300 °C. Two specimens of various temperatures at strain amplitude of 0.6% were selected for further analysis. There exists some cracks in HAZ and adjacent to HAZ besides the failure location, reflecting the failure mode at 300 °C is competitive.

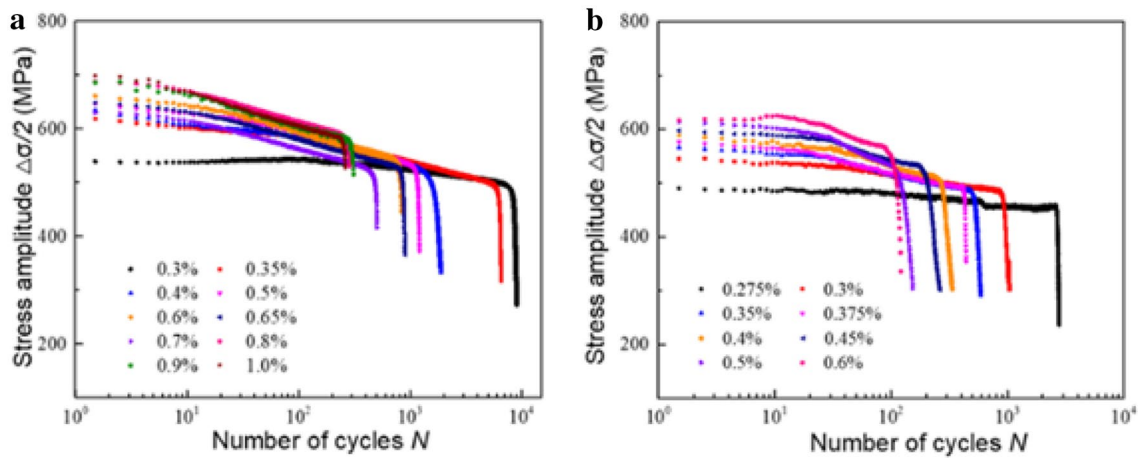

Figure 4 Cyclic deformation behavior at different temperatures: **a** RT, **b** 300 °C

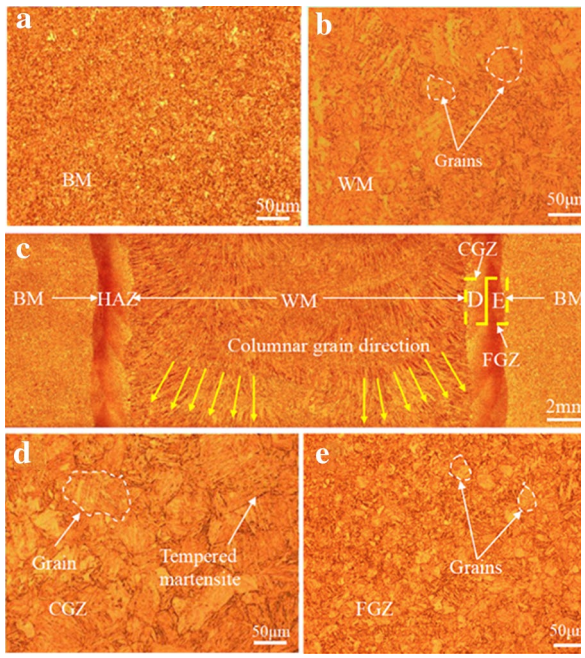

Figure 5 Structure of the welded joint: **a** microstructure of BM, **b** macrostructure of WM, **c** the overall macrostructure of the whole welded joint, **d** microstructure of course grain zone, **e** microstructure of fine grain zone

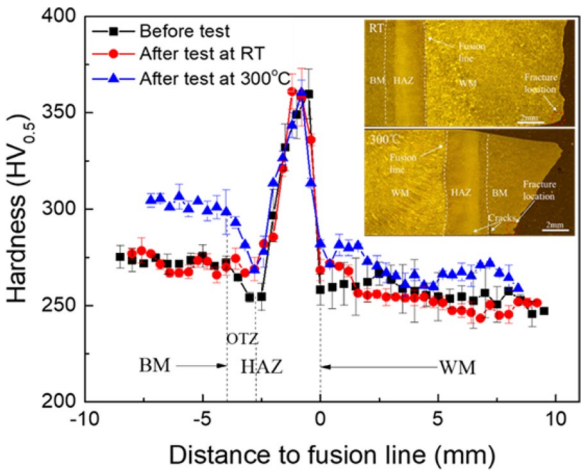

Figure 6 Failure location and micro-hardness distribution before and after test

Figure 6 shows the micro-hardness distribution of welded joint before and after LCF test, the micro-hardness of WM before test has a good match with that of BM. It is clearly noted that the micro-hardness of OTZ in HAZ drops remarkably in the HAZ as the repeated over tempering during the welding process. Some researchers suggested the sharply micro-hardness drop zone may be the most vulnerable area in the LCF test at room temperature. So much attention should be paid to this zone. Finally, the width of HAZ is determined about 4.0 mm, which could be utilized to confirm the precise failure location of the specimen.

The hardness test showed that WM became a little bit softer comparing to that before test after LCF test at RT, while the micro-hardness of HAZ rose up to the same level with the BM accompanied with soft zone in OTZ vanished. So the WM become the weaker part of the whole joint for LCF test at RT, leading to failure happen in WM. For the specimen at 300 °C, BM and HAZ exhibited a sharp hardening behavior while the weld metal displayed a slightly hardening behavior. However, the soft zone still existed in OTZ. The different hardening and softening behavior in various zones may be tightly associated to the load each zone takes up and affecting the final fracture behavior. The fracture location was 4.4 mm from the fusion line, so the specimen at 300 °C could be furtherly confirmed to fail at OTZ near the BM rather than in the soft zone.

3.5 Fracture Morphology

Fracture surface were observed for two failed specimens, showing in Figure 7 and Figure 8, respectively. The overall morphology of the specimen failed at WM at room temperature is presented in Figure 7(a). It can be clearly observed that specimen exhibits a multi-surface crack initiation feature. One of the surface crack initiations is magnified and shown in Figure 7(b) and no obvious inclusion exists, which indicates the surface crack initiation can be attributed to extrusion and invasion mechanism induced by the movement of slip bands. Obvious fatigue striations in the crack propagation area can be observed in Figure 7(c). Generally, the slip of the dislocations in the plastic zone ahead of the crack tip is deemed to be responsible for the occurrence of the fatigue striations. An internal inclusion with diameter of 40 μm is magnified and displayed in Figure 7(d) and a plane can be observed around the inclusion, the EDS analysis result is shown in the inserted table. We can conclude that the internal inclusion is not a crack initiation as it occurs in the final fracture area. The competition between the surface and inner initiation due to an internal inclusion have been investigated by Hu et al. [36], they deem that the LCF lifetime is more sensitive to surface defects, while crack nucleates from internal inclusion has a longer fatigue lifetime due to smaller stress concentration at crack tips.

Figure 8(a) exhibits the overall SEM micrograph of the specimen failed at OTZ at 300 °C, the surface crack area, the crack propagation area and the final fracture area

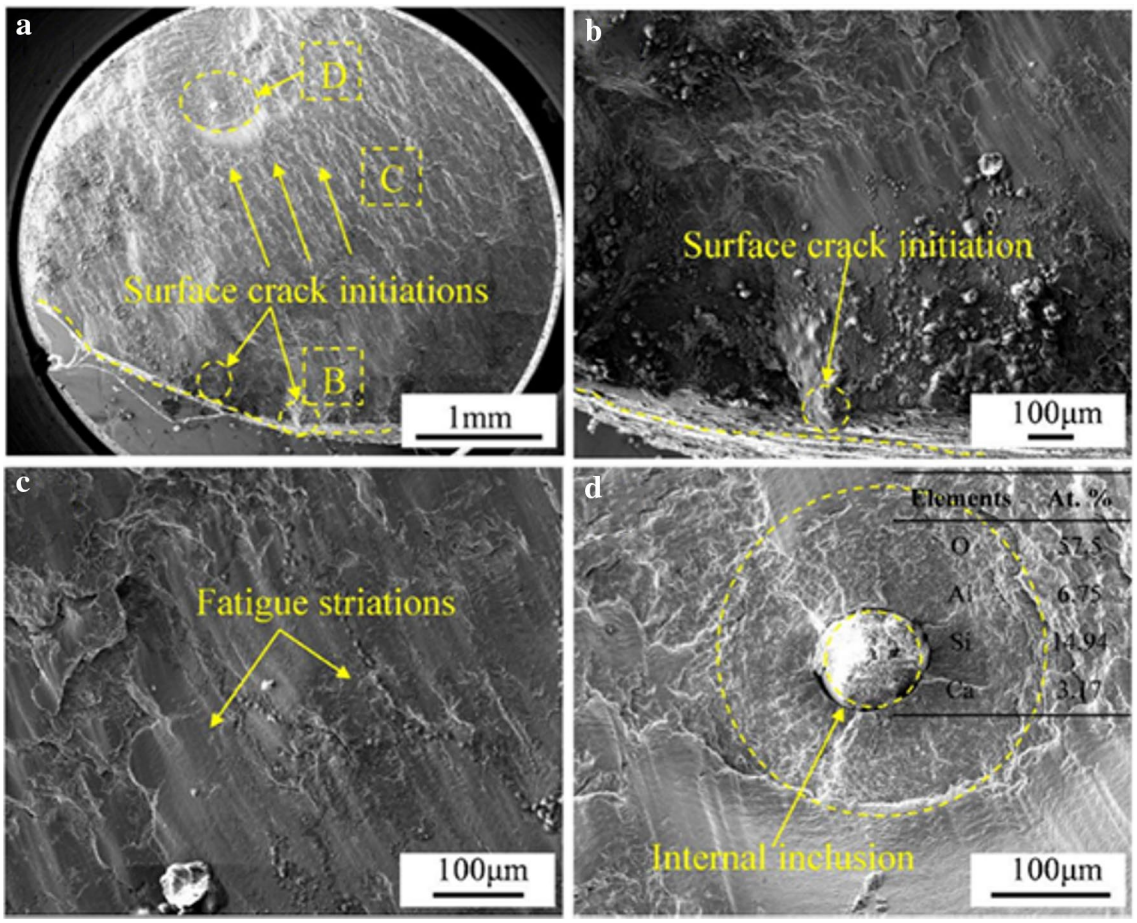

Figure 7 Fracture morphology of the specimen failed at WM at room temperature: **a** the overall morphology of fracture surface, **b** magnified micrograph of one surface crack initiation, **c** fatigue striations near the surface crack initiation, **d** internal inclusion in the final fracture zone

can be easily distinguished. Two obvious surface crack initiations are magnified and depicted in Figure 8(b) and (c), respectively. For one surface crack initiation in Figure 8(b), an obvious inclusion is observed and the chemical composition of the inclusion is MgO and Al_2O_3. While no inclusion exists in another surface crack initiation in Figure 8(c), which indicates the extrusion and invasion of slip bands plays a dominate role here. In Figure 8(d) presents the fatigue striations induced by the surface crack initiations, which is clearer compared to the Figure 7(c), reflecting the ductility of OTZ at 300 °C is better than that of the WM at RT.

3.6 Discussion

According to Table 2, the joint has smaller fatigue ductility coefficient $\left(\varepsilon_f'\right)$ and fatigue ductility exponent (c) accompanied with bigger cyclic strength coefficient (n') and the cyclic hardening exponent (K') at 300 °C, which means the joint experiences more significantly strain hardening effect and has worse plastic deformation resistance than that of room temperature, indicating the microstructure deteriorates faster thus resulting the reduction of fatigue life with the increasing temperature.

As shown in Figure 6, the middle of the WM suffers softening and the cyclic strain hardening effect occurs in OTZ. As fatigue parameters mentioned above, the joint is more sensitive to the micro-hardness distribution at room temperature, which resulting in the failure in the middle of WM. When it comes to 300 °C, the fracture occurs in OTZ near the BM while existing some cracks in HAZ, the crack and fracture location corresponding to the soft zone in OTZ and the fracture location where consists of surface inclusion, respectively. It has been found that surface cracks initiate not only from the damaged grain boundaries but also from geometrically discontinuous portions such as slip steps [37]. As can be seen from Figure 6, the BM and HAZ exhibited a sharp hardening behavior while the soft zone still exists, but the joint fails in OTZ near BM where consists

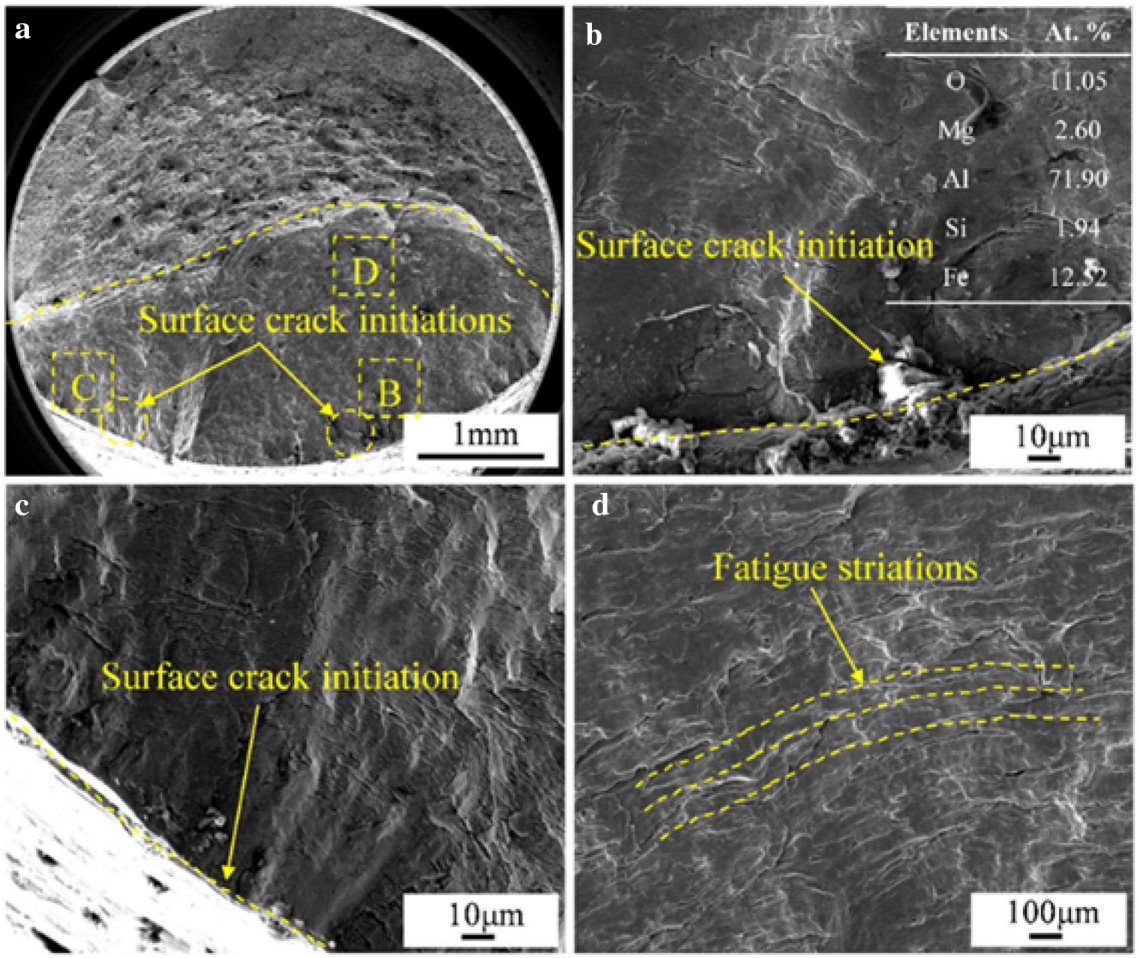

Figure 8 Fracture morphology of the specimen failed at OTZ at 300 °C: **a** the overall micrograph of the fracture surface, **b** magnified micrograph of one surface crack initiation, **c** magnified micrograph of another surface crack initiation, **d** fatigue striations in the crack propagation zone

of surface inclusion rather than in the soft zone in OTZ. As the softest part in HAZ, OTZ has great hardness differences with the surrounding microstructure. Thus, lots of microcracks are found at OTZ. However, their crack growth rates are much slower than the crack leading to failure with inclusion on the surface. This indicated that the joint is more sensitive to the distributed surface inclusion at 300 °C.

4 Conclusions

LCF tests were conducted on the bainite welded joint at two temperatures, the failure locations at two temperatures were analyzed. Some conclusions are drawn as follows:

(1) The fatigue life curves at two temperatures both can be described well by the Manson-Coffin relationship. Fatigue parameters derived from fitting curves indicates that the joint has worse plastic deformation resistance and experiences more significantly strain hardening effect at 300 °C.
(2) Except initial stabilized stress response at single low strain amplitude, a gradual cyclic softening followed by a sharp softening behavior is observed at all strain amplitudes at both temperatures.
(3) The joint fails at middle of WM at RT, which attributed to the softening effect of WM combined with cyclic strain hardening effect in OTZ. When it comes to 300 °C, the heterogeneous distributed surface inclusion is responsible for the fracture transition to OTZ near BM rather than the soft zone in OTZ, reflecting the joint is more sensitive to the surface inclusion.

Authors' Contributions
FL was in charge of the whole trial. KX contributed the central idea, analysed most of the data and wrote the initial draft of the paper. XW, and HC

contributed to refining the ideas, carrying out additional analyses and finalizing this paper. All authors read and approved the final manuscript.

Authors' Information

Ke Xu, born in 1980, is currently a PhD candidate at *School of Materials Science and Engineering*, *Shanghai Jiao Tong University*, *China*.

Xiongfei Wang, born in 1992, is currently a master candidate at *School of Materials Science and Engineering, Shanghai Jiao Tong University*, *China*.

Haichao Cui, born in 1979, is currently an associate senior engineer at *School of Materials Science and Engineering*, *Shanghai Jiao Tong University*, *China*. He received his PhD degree from *Shanghai Jiao Tong University*, *China*, in 2012.

Fenggui Lu, born in 1975, is currently a professor and a PhD candidate supervisor at *School of Materials Science and Engineering*, *Shanghai Jiao Tong University*, *China*.

Competing Interests

The authors declare that they have no competing interests.

Funding

Supported by National Natural Science Foundation of China (Grant Nos. 51675336, U1660101, and 51775338).

Received: 13 August 2018 Accepted: 18 March 2019
Published online: 28 March 2019

References

[1] Y Liu, H Li, S Sun, et al. Enhanced air dispersion modelling at a typical Chinese nuclear power plant site: Coupling RIMPUFF with two advanced diagnostic wind models. *Journal of Environmental Radioactivity*, 2017, 175: 94-104.

[2] E Shahi, F S Alavipoor, S Karimi. The development of nuclear power plants by means of modified model of Fuzzy DEMATEL and GIS in Bushehr, Iran. *Renewable and Sustainable Energy Reviews*, 2018, 83: 33-49.

[3] G R Odette, M J Alinger, B D Wirth. Recent developments in irradiation-resistant steels. *Annu. Rev. Mater. Res.*, 2008, 38(1): 471-503.

[4] X Hu, L Huang, W Yan, et al. Low cycle fatigue properties of CLAM steel at 823 K. *Materials Science and Engineering: A*, 2014, 613(34): 404-413.

[5] P Liu, F Lu, X Liu, et al. Study on fatigue property and microstructure characteristics of welded nuclear power rotor with heavy section. *Journal of Alloys and Compounds*, 2014, 584(25): 430-437.

[6] H Miao, Q Mei, J Yuan, et al. Low cycle fatigue and strengthening mechanism of cold extruded large diameter internal thread of Q460 steel. *Chinese Journal of Mechanical Engineering*, 2016, 29(3): 556-563.

[7] M D Callaghan, S R Humphries, M Law, et al. Energy-based approach for the evaluation of low cycle fatigue behaviour of 2.25Cr–1Mo steel at elevated temperature. *Materials Science and Engineering: A*, 2010, 527(21-22): 5619-5623.

[8] R Liu, Z J Zhang, P Zhang, et al. Extremely-low-cycle fatigue behaviors of Cu and Cu–Al alloys: Damage mechanisms and life prediction. *Acta Materialia*, 2015, 83: 341-356.

[9] P J Phillips, R R Unocic, M J Mills. Low cycle fatigue of a polycrystalline Ni-based superalloy: Deformation substructure analysis. *International Journal of Fatigue*, 2013, 57(12): 50-57.

[10] L Zhao, S Zheng, J Feng. Fatigue life prediction under service load considering strengthening effect of loads below fatigue limit. *Chinese Journal of Mechanical Engineering*, 2014, 27(6): 1178-1185.

[11] Q Wu, F Lu, H Cui, et al. Role of butter layer in low-cycle fatigue behavior of modified 9Cr and CrMoV dissimilar rotor welded joint. *Materials & Design*, 2014, 59(7): 165-175.

[12] B Fekete. New energy-based low cycle fatigue model for reactor steels. *Materials & Design*, 2015, 79: 42-52.

[13] W Kosman. Thermal analysis of cooled supercritical steam turbine components. *Energy*, 2010, 35(2): 1181-1187.

[14] L Cui, P Wang. Two lifetime estimation models for steam turbine components under thermomechanical creep–fatigue loading. *International Journal of Fatigue*, 2014, 59(2): 129-136.

[15] J Veerababu, S Goyal, R Sandhya, et al. Low cycle fatigue behaviour of Grade 92 steel weld joints. *International Journal of Fatigue*, 2017, 105: 60-70.

[16] K Mariappan, V Shankar, R Sandhya, et al. Dynamic strain aging behavior of modified 9Cr–1Mo and reduced activation ferritic martensitic steels under low cycle fatigue. *Journal of Nuclear Materials*, 2013, 435(1): 207-213.

[17] G Dundulis, R Janulionis, A Grybėnas, et al. Numerical and experimental investigation of low cycle fatigue behaviour in P91 steel. *Engineering Failure Analysis*, 2017, 79: 285-295.

[18] A Chauhan, D Litvinov, T Gräning, et al. High-temperature low-cycle fatigue behavior and microstructural evolution of an improved austenitic ODS steel. *Journal of Materials Research*, 2018, 33(12): 1-8.

[19] V Shankar, K Mariappan, R Sandhya, et al. Understanding low cycle fatigue and creep–fatigue interaction behavior of 316 L(N) stainless steel weld joint. *International Journal of Fatigue*, 2016, 82(5): 487-496.

[20] K J C Chou, J C Earthman. Characterization of low-cycle fatigue damage in Inconel 718 by laser light scanning. *Journal of Materials Research*, 1997, 12(8): 2048-2056.

[21] R Mishnev, N Dudova, R Kaibyshev. Low cycle fatigue behavior of a 10Cr–2W–Mo–3Co–NbV steel. *International Journal of Fatigue*, 2016, 83: 344-355.

[22] K Guguloth, S Sivaprasad, D Chakrabarti, et al. Low-cyclic fatigue behavior of modified 9Cr–1Mo steel at elevated temperature. *Materials Science and Engineering: A*, 2014, 604: 196-206.

[23] P Verma, N C S Srinivas, S R Singh, et al. Low cycle fatigue behavior of modified 9Cr–1Mo steel at room temperature. *Materials Science and Engineering: A*, 2016, 652: 30-41.

[24] P Verma, N C S Srinivas, S R Singh. Low cycle fatigue behavior of modified 9Cr-1Mo steel at 300 °C. *Materials Science and Engineering: A*, 2018, 715: 17-24.

[25] X Wang, C Shao, X. Liu, et al. Transition and fracture shift behavior in LCF test of dissimilar welded joint at elevated temperature. *Journal of Materials Science & Technology*, 2018, 34(4): 720-731.

[26] Q Guo, F Lu, X Liu, et al. Correlation of microstructure and fracture toughness of advanced 9Cr/CrMoV dissimilarly welded joint. *Materials Science and Engineering: A*, 2015, 638: 240-250.

[27] W Liu, X Liu, F Lu, et al. Creep behavior and microstructure evaluation of welded joint in dissimilar modified 9Cr–1Mo steels. *Materials Science and Engineering: A*, *2015*, 644: 337-346.

[28] W Liu, F Lu, Y Wei, et al. Special zone in multi-layer and multi-pass welded metal and its role in the creep behavior of 9Cr 1Mo welded joint. *Materials & Design*, 2016, 108: 195-206.

[29] S Wang, Q Ma, Y Li. Characterization of microstructure, mechanical properties and corrosion resistance of dissimilar welded joint between 2205 duplex stainless steel and 16MnR. *Materials & Design*, 2011, 32(2): 831-837.

[30] Y Li, Z Cai, K Li, et al. Investigation of local brittle zone in multipass welded joint of NiCrMoV steel with heavy section. *Journal of Materials Research*, 2018, 33(8): 923-934.

[31] M L Zhu, L L Liu, F Z Xuan. Effect of frequency on very high cycle fatigue behavior of a low strength Cr–Ni–Mo–V steel welded joint. *International Journal of Fatigue*, 2015, 77: 166-173.

[32] M L Zhu, F Z Xuan, G Z Wang. Effect of microstructure on fatigue crack propagation behavior in a steam turbine rotor steel. *Materials Science and Engineering: A*, 2009, 515(1): 85.

[33] Y N Du, M L Zhu, F Z Xuan: Transitional behavior of fatigue crack growth in welded joint of 25Cr2Ni2MoV steel. *Engineering Fracture Mechanics*, 2015, 144: 1-15.

[34] M L Zhu, D Q Wang, F Z Xuan. Effect of long-term aging on microstructure and local behavior in the heat-affected zone of a Ni–Cr–Mo–V steel welded joint. *Materials Characterization*, 2014, 87: 45-61.

[35] X Liu, Z Cai, X Deng, et al. Investigation on the weakest zone in toughness of 9Cr/NiCrMoV dissimilar welded joint and its enhancement. *Journal of Materials Research*, 2017, 32(16): 3117-3127.

[36] D Hu, T Wang, Q Ma, et al. Effect of inclusions on low cycle fatigue lifetime in a powder metallurgy nickel-based superalloy FGH96. *International Journal of Fatigue*, 2019, 118: 237-248.

[37] M Kamaya. Fatigue properties of 316 stainless steel and its failure due to internal cracks in low-cycle and extremely low-cycle fatigue regimes. *International Journal of Fatigue*, 2010, 32(7): 1081-1089.